Concentric Push-Pull Robots: Planar Modeling and Design

Kaitlin Oliver-Butler *Member, IEEE*, Jake Childs *Student Member, IEEE*, Adam Daniel, and Caleb Rucker *Member, IEEE*

***Abstract*— Concentric push-pull robots (CPPR) combine the simplicity, miniaturization potential, and open lumen of concentric-tube robots with the kinematic advantages and stability of push-pull multi-backbone designs. A CPPR robot segment is made from a pair concentric tubes with notches asymmetrically cut into their sides in opposing directions. The two tubes are attached to one another at their tips, and push-pull translation of the tube bases relative to each other changes the curvature along the length of the combined tube pair. Custom variable curvature shapes are possible by varying the notch parameters along the tubes. In this paper, we present a planar variable-curvature mechanics model for the actuated segment shape and a method for designing the notch pattern to achieve a desired planar, variable-curvature shape with maximal stiffness within specified strain limits. Experiments validate accuracy for various shapes, materials, and cross sections, showing that the design method achieves a variety of desired shapes. We also demonstrate a multi-segment robot made from multiple tube pairs that can independently rotate and actuate, increasing the robot DOF.**

Keywords– Flexible Robots, Kinematics, Soft Robot Materials and Design, Continuum Robots

I. Introduction

The reach of modern robotics has expanded beyond the safety cages of a factory floor, and with this transition, novel devices have been created to attain broader capabilities and meet the demands of new environments. Continuum and soft robotics arose from a desire to utilize a material's flexibility to create robots that take organic, bending actuated shapes. Benefits of this approach include intrinsic safety for human interaction [1], [2], gripping of delicate or irregularly shaped objects [3], [4], [5], and the ability to be made at slender, millimeter-scale sizes for access in hard-to-reach areas [6], [7]. They have been used in applications from aerospace [8] to medicine [9]. Additionally, various means of actuating continuum robots exist, many of which allow the actuators to remain at the base of the robot– some systems pull on tendons down the length of an elastic element to generate bending [10], [11], [12], others have pneumatic chambers that are actuated by pressurization [13], [14], [15], and others still combine elastic elements that interact with each other, arriving at various equilibrium positions due to asymmetry in the components or their configuration [16], [17], [18]. Concentric-tube robots (CTRs) [19], [20], [21], [6] and multi-backbone robots [22], [23] fall into this latter category. Our proposed concept, a concentric push-pull robot (CPPR), combines some beneficial characteristics from both concentric-tube and multi-backbone push-pull approaches. As shown in Figure 1 and described in the caption, a single robot segment is made from two concentric tubes with a pattern of cutout segments. After fixing the tube tips together, push-pull actuation generates bending. The cutout profile can be designed for specific shape or workspace objectives, and multiple tube pairs can be combined concentrically.

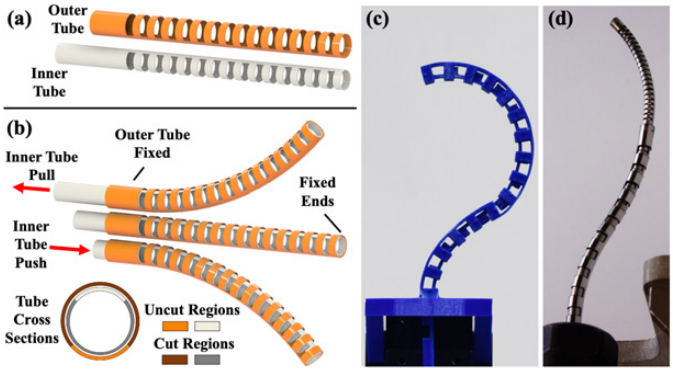

Fig. 1: **(a)** A CPPR is composed of at least two tubes with a pattern of cutout segments down the length. **(b)** The tips of the two tubes are fixed together such that the notches of the two tubes are opposed, 180° apart. Pushing or pulling on the tubes with respect to one another then generates bending. **(c)** The notch pattern can be varied down the length and designed to achieve various shapes. **(d)** A 2-pair multi-segment CPPR demonstrates 5 degrees of freedom by actuating each segment independently.

We first introduced the CPPR concept in [24] and explored its potential use to steer endoscopic tools in [25]. As demonstrated in [25], endoscopic deployment is one target application for CPPRs, where they can be used as an actuatable distal tip on a long, flexible tube transmission deployed through existing endoscope tool channels. Its compact form factor and open lumen then allows passage of standard tools such as graspers through its central lumen. This provides enhanced dexterity to the surgeon with minimal change in equipment. Its design is inspired by a tendon-driven wrist design by York et al. in [26] and Swaney et al. in [27], which is also studied by Eastwood et al. in [28], [29]. These devices and the CPPR both use asymmetric material removal to shift the neutral axis

This material was funded in part by the National Science Foundation under CAREER Award #1652588. Any opinion, findings, and conclusions or recommendations expressed in this material are those of the authors and do not necessarily reflect the views of the National Science Foundation.

K. Oliver-Butler, J. Childs, A. Daniel, and D. C. Rucker are with the University of Tennessee, Knoxville, TN 37996, USA (e-mail: caleb.rucker@utk.edu).

of a primary tube; however, instead of a pull-wire, an CPPR uses a second asymmetrically notched tube fixed to the tip of the first one to induce bending in the structure, as shown in Figure 1. Compared to the single tendon-driven wrists, the double tube structure strengthens the device in bending and torsion and adds bi-directional actuation capability (push-pull), which increases workspace and force capacity. Compared to conventional tendon-driven or multi-backbone continuum robot designs with internal routing structures such as disks, the concentric push-pull tube construction is potentially simpler and allows more room in the inner lumen. But multiple tube pairs are required to achieve independent control of position and orientation. Compared to concentric tube robots (CTRs) using precurved tubes that are rotated, the stiffness and strength are reduced due to the removal of wall material, and more more tubes are needed to achieve the same degrees of freedom (3 DOF for a single CPPR tube pair, vs. 4 DOF for a CTR tube pair). However, the kinematic control is less complicated, the bending range of motion is potentially larger, and the issue of unstable snapping motions is eliminated.

Selective removal of tube wall material has been used to modify the properties of metal and plastic tubes for a number of purposes in robotics, such as shifting the neutral axis [26], [28], generating high angulation for compact devices [29], [30], [31], reducing bending stiffness for tendon-actuated designs [32], [33], [34], creating continuously-variable stiffness manipulators with multiple tubes [35], and increasing the torsional stability of concentric tube robots [36], [37]. The CPPR concept leverages asymmetric material removal to enable the tubes themselves to function as actuation transmission elements, which simplifies the design and enables bending through push-pull actuation without any additional components. This concept is analogous to push-pull multi-backbone actuation, but in a different form factor which preserves a central working channel through which flexible instruments can be deployed. It also inherits the simplicity and ease of miniaturization of precurved concentric-tube robots [19], [20], [21], [6] while eliminating the issue of elastic instability [38] and enabling more straightforward control of curvature.

In addition to its compact form factor and straightforward actuation principle, the CPPR represents a versatile and robust design concept that can be created with a variety of materials and through both additive and subtractive fabrication methods (milling, wire EDM, laser-cutting, etc.). Additive manufacturing of concentric tube robots has been explored by Motorimoto et al in [39], and Amanov et. al. use it to generate patient-specific manipulators in [40]. Similar customization frameworks can be used for the design of the CPPR in principle, but a model-based approach to design a CPPR to achieve a specific desired curve is needed first. This is our main contribution in this paper.

A. Outline and Contributions

In prior work in [24], we introduced the CPPR concept, derived an approximate constant-curvature kinematic model, and tested it on a 3D-printed prototype. Additionally, a small-scale prototype for endoscopic use was built and deployed inside a bronchoscope as a precursor to robotic implementation [25]. In this paper, motivated by the opportunity to customize manipulator workspace and dexterity for specific tasks and applications, we first expand the kinematic analysis to include variable curvature, planar shapes. Then we provide an algorithm to design the notch parameters to achieve a desired shape in Section III, accounting for material strain limits to achieve a robust and feasible design with maximal stiffness. We built and tested variable-curvature CPPR prototypes with multiple notch patterns, cross-sections, and materials using the proposed design method, showing in Section IV that the results have good agreement between both the desired curvature and the experimental prototype's actuated shape as well as the new kinematics model and experiments. Section VI discusses some of the considerations and practicalities in building an CPPR and offers some guidance on design. It also includes a proof-of-concept demonstration of a multi-segment CPPR. We conclude our work and discuss future activities in Section VII.

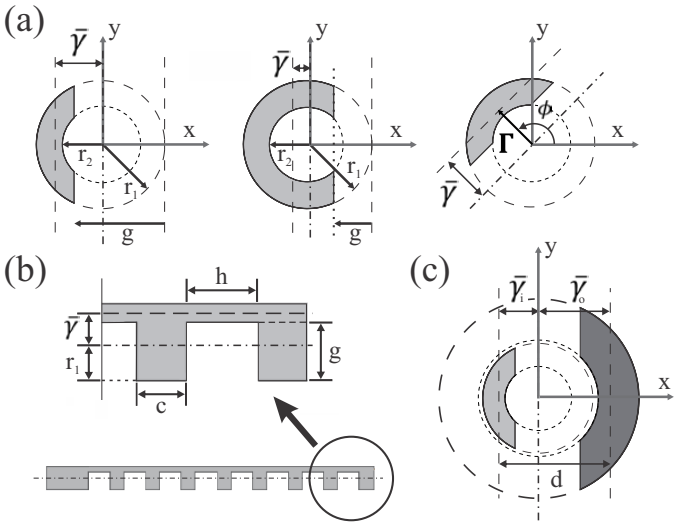

Fig. 2: The neutral axis offset and notch parameters of a single tube are shown in **(a)** and **(b)**, while **(c)** shows the cross section of two nested tubes. Both the inner and outer tubes have n notches. The wall thicknesses are exaggerated for clarity. **(a)** A close-up of a single notch shows the neutral axis offset, $\overline{\gamma}$, based on notch depth, g, notch angle, ϕ, tube outer radius, r_1, and tube inner radius, r_2. **(b)** A close-up of the profile of the notched tube shows the notch length, notch depth, and notch spacing parameter definitions. **(c)** The cross section of the assembled CPPR at a notched section, which shows the tubes nested inside each other.

II. Variable Curvature Model

Each notch on the CPPR acts as an individual bending hinge, and the overall manipulator behavior is the result of the summation of their deflections. The bending plane of the robot passes through the tube center and is orthogonal to the neutral axes of the two notched tubes. The magnitude of deflection is determined by the stiffness of the notches in each tube. The variations of notch bending plane and stiffness along the

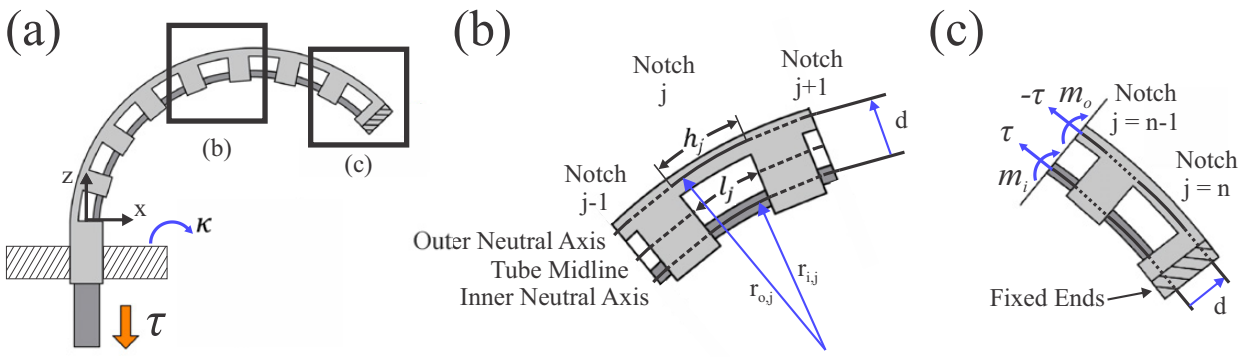

Fig. 3: (a) The coordinate definitions, where pulling on the inner tube creates a positive curvature, κ. **(b)** A close-up of the j^{th} notch, showing the relationship between inner and outer tube curvatures and the manipulator centerline. **(c)** A free-body diagram of the tip, used in our force and moment balances.

backbone are determined by the notch parameters, as shown in Figure 2: the number (n), length (h), spacing (c), depth (g), and orientation/angle of the notch in the cross sectional plane (ϕ). The parameters of h and c determine when the notches will self-interfere at the edges of the workspace, which occurs when a notch bends so far that the opposite edges of the notch come into contact, closing the hinge formed by the notch. From that point, material contact prevents it from bending any further. Their relationship dictates how closely an arc can approximate the overall shape of the manipulator (i.e., if h is small and c is large, the manipulator will have long, straight sections, whereas if the opposite were true, the straight sections would be small and negligible). The notch depth, g, determines the offset of the neutral axis (and thus the location of the bending plane) as well as the strain in the notch, which is typically the limiting factor for the workspace unless one uses high-strain materials such as superelastic nitinol. The orientation (notch angle), ϕ, determines the rotation of the bending plane about the axis of the tube.

The notched tubes are aligned concentrically, such that the two backbones are parallel to each other but on opposite sides of the manipulator (i.e., $\phi_o = \pi$ and $\phi_i = 0$) (see Figure 1) with the tips rigidly attached to each other. When the base of one tube translates with respect to the other, the tubes are placed in agonist-antagonist compression and tension, which, in turn, causes bending in the device. When the notches are uniform along the length, the manipulator shape can be approximated by a constant-curvature arc. However, when the notches are varied along the length, the actuated shape is non-constant curvature, which can be exploited to design the kinematics of the manipulator for a given task.

A. Assumptions

We list various assumptions in our approach below:

- While the inner and outer tubes may have different values for g and ϕ at each notch, we assume they share the same values of n, h, and c. This reduces the design parameter space and model complexity without a significant loss of model generality or versatility of the possible designs.
- We assume that the deformation over a single notch is dominated by pure bending, that the curvature is constant over each notch, and that the internal moment is equal to the curvature times the bending rigidity.
- As the device is actuated, some of the rigid, non-notched segments will overlap with notched segments of the other tube, as is visible in Figure 1. We assume that the tube clearances are sufficient to allow the rigid segments to reorient themselves such that interference and binding do not occur when the notches are no longer aligned. This allows the tubes to easily slide past each other even when maximally bent. We have not observed any issues due to notch misalignment during actuation of our prototypes.
- In our kinematic derivation, we also neglect the geometric nonlinearities associated with notch misalignment on the mechanics. I.e., the moment balance is written in the rest configuration where the notches are aligned, rather than the actuated configuration when they are misaligned. The simplicity/accuracy trade-off of this assumption is good as evidenced by our experiments.
- The kinematics model assumes that bending only occurs in the notched portions, and the non-notched portions behave in a perfectly rigid manner. To ensure sufficient rigidity of the uncut sections, we recommend that the minimum value of c be at least the radius of the outer tube. To ensure that the notched sections are sufficiently flexible relative to the rigid sections, we have observed that notch depths greater than 50% of the outer diameter should be used, which is not a very restrictive constraint as material strain limits typically result in designs with deeper notches regardless.
- We also assume that friction is insignificant. This assumption becomes less accurate as the manipulator becomes more curved, but is reasonably accurate over the workspace of the prototypes in this paper.
- Finally, we assume that the notch cross section has at least one axis of symmetry orthogonal to its neutral axis. This enables the CPPR to be made with wide array of non-circular shapes, as we demonstrate in our experiments in Section IV.

B. Neutral Axis Offset Geometry

The notch depth, g, is the most important factor in determining the stiffness of a given notched section, and varying it along the tube generates a variable curvature shape. This parameter determines the second moment of area, I, of the tube's notched cross section, as well as the neutral axis offset from the tube centerline, $\mathbf{\Gamma}$, which we define as a vector within the plane of the cross section:

$$\mathbf{\Gamma} = \bar{\gamma} \begin{bmatrix} \cos(\phi) \\ \sin(\phi) \end{bmatrix}, \tag{1}$$

where ϕ is the notch angle measured from the x-axis and $\bar{\gamma}$ is the magnitude of the offset, as shown in Figure 2. In this paper, we consider only planar segment curves in the $x-z$ plane, so we restrict ϕ to be either 0 or π depending on the direction of the cut. Thus, only the x-component of $\mathbf{\Gamma}$ is nonzero, and we write

$$\gamma = \bar{\gamma}\cos(\phi),$$

where here and throughout the rest of the paper, the symbol γ denotes the signed neutral axis location in the x direction, whereas $\bar{\gamma}$ denotes the absolute value of γ. The equations for $\bar{\gamma}$ for a circular segment cross section made by cutting the notches can be found in [24], [41], [27]. The CPPR can have a non-circular cross section, as demonstrated in the experiments, provided that the cross-section has an axis of symmetry normal to the neutral axis of the cross section. Non-circular tube cross sections may offer advantages in being easier to assemble – due to automatic rotational alignment – and in making the manipulator stronger in torsion, as non-circular tubes are constrained not to rotate with respect to each other everywhere along the length.

C. Backbone Curvature Relationships at Each Notch

At a particular notch, the relationship between the curvature of the inner and outer tube backbones are dictated by their opposing notches, thus we state

$$\phi_i = \phi_o - \pi \tag{2}$$

where ϕ_o and ϕ_i are the angles of the outer and inner tube neutral axis offsets, respectively, measured from the positive x-axis. This implies that $sgn\,(\gamma_o) = -sgn\,(\gamma_i)$. From that relationship, we also define the signed distance between the two, d, as

$$d = \gamma_i - \gamma_o, \tag{3}$$

which is a fixed constant for each notch pair based on the notch geometry. (We later use a subscript j to denote a value associated with the j^{th} notch, but we omit it here for notational simplicity.) This constant then defines the relationship between inner and outer backbone curvatures, as illustrated in Figure 3(b):

$$r_o = r_i + d$$

thus

$$\frac{1}{\kappa_o} = \frac{1}{\kappa_i} + d,$$

where r_o and r_i are the radii of curvature of the outer and inner tubes, respectively, and κ_o and κ_i are the corresponding curvatures, as illustrated in Figure 3.

We assume that the curvatures are constant over the length of a single notch and that the curves of the tubes' neutral axes share a common center of curvature outside the body of the manipulator (which merely excludes curvatures so large that self-contact would occur). These assumptions imply the following relationships and constraints:

$$r_o = r - \gamma_o \qquad r_i = r - \gamma_i$$

where r is the radius of curvature of the robot centerline. This results in a relationship between the curvatures

$$\kappa_o = \frac{\kappa}{1-\gamma_o\kappa} \qquad \text{and} \qquad \kappa_i = \frac{\kappa}{1-\gamma_i\kappa}, \tag{4}$$

in which the denominators can never be zero due to the above restrictions. Note that the curvatures and radii of curvature are allowed to be negative, which would indicate that the segment is curving in the opposite direction than shown in Figure 3(a).

D. Mechanics at a Notch

As shown in Figure 3(a), pulling on the inner tube is defined as positive actuation. With that definition, summing the moments about the outer tube's neutral axis as shown in the free-body diagram in Figure 3(c) gives

$$-d\tau + m_o + m_i = 0 \tag{5}$$

where τ is the tension carried by the inner tube, d is defined as above for a notch, and m_i and m_o are the internal moments of the inner and outer backbones, respectively, carried in an inner-outer notch pair at an arc length location coincident with a notch, which we call "at" a notch moving forward. Note that there are no transverse shear loads, and while there is an axial load in the backbone, we assume its deflection component is negligible compared to the deflection in bending. We can then use the linear constitutive law of classical beam mechanics to relate the internal moments in the backbone to their respective curvatures:

$$m_i = E_i I_i \kappa_i \quad \text{and} \quad m_o = E_o I_o \kappa_o,$$

where E is Young's Modulus and I is the second moment of area. Using this and the relationship between the tube curvatures in Equation (4), we can rewrite (5) in terms of centerline curvature as

$$-d\tau + E_o I_o \frac{\kappa}{1-\gamma_o\kappa} + E_i I_i \frac{\kappa}{1-\gamma_i\kappa} = 0. \tag{6}$$

In terms of only the outer tube curvature and for the j^{th} notch, τ is:

$$\tau = \left(E_o I_{o,j} \kappa_{o,j} + E_i I_{i,j} \frac{\kappa_{o,j}}{1 - d\kappa_{o,j}} \right) d_j^{-1}. \tag{7}$$

If tension is a known input, this equation can be used with Equations (9) through (13) below to attain the robot position.

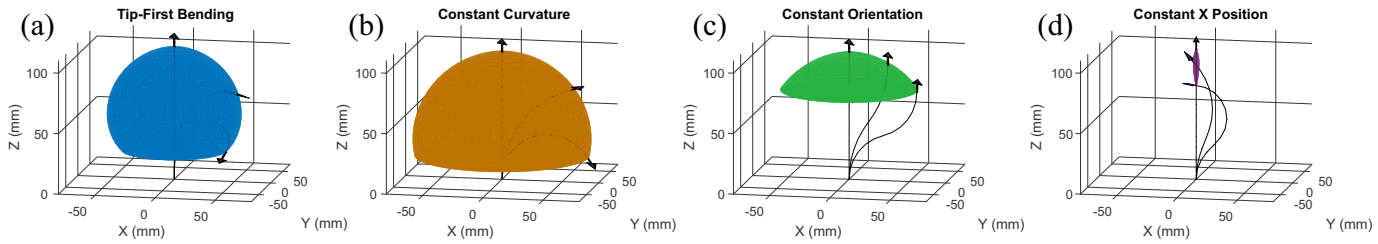

Fig. 4: Workspaces of CPPR Designs. All four designs share the same material properties, tube diameters, and wall thicknesses. The workspaces simulate actuation and axial rotation of the robots, and arrows on the end of the manipulator shape indicate the tip direction. As this shows, the workspace and tip orientation can be drastically altered by the actuated shape of the robot. The workspace seen in **(a)** is that of Design 2 from the experiments in Section IV. All workspace diagrams were generated in MATLAB.

E. Kinematics of a Variable-Curvature Segment

Often, displacement is dictated by the actuation system instead of tension, so we seek a kinematic relationship between the relative displacement of the tubes and the shape of a variable-curvature segment with multiple notches down its length. The actuation variable, q, is the relative displacement of the tube bases. The outer tube is defined as fixed in Figure 3, and pulling on the inner tube is defined as the positive direction of q, so the change in relative displacement is equal to the change in the length of the inner tube's path through the outer tube, which can be defined as:

$$q = s_i - s_{i,act}$$

where s_i is the fixed length of the inner tube backbone and $s_{i,act}$ is the changing length of the path through the outer tube, which shortens and lengthens as the outer backbone bends. These are calculated as

$$s_i = \sum_{j=1}^{n} (c_{i,j} + h_{i,j})$$

and

$$s_{i,act} = \sum_{j=1}^{n} (c_{o,j} + s_{a,j})$$

where $s_{a,j}$ is the length of the inner tube path through the bending portions of the j^{th} outer tube notches. Solving for q, the c terms cancel because they are constant and equal for both tubes. The equation can be further simplified by the fact that $h_{i,j} = h_{o,j} = h_j$, yielding

$$q = \sum_{j=1}^{n} (h_j - s_{a,j}) .$$

The remaining $s_{a,j}$ terms can be defined in terms of the outer tube geometry by using the geometric relationships based on arc geometry

$$s_{a,j} = r_{i,j} h_j \kappa_{o,j} \qquad \text{and} \qquad d_j = r_{o,j} - r_{i,j}.$$

Finally, the expression for q can be expressed in terms of the curvatures:

$$q = \sum_{j=1}^{n} d_j h_j \kappa_{o,j} \tag{8}$$

where h_j is the notch length of the j^{th} notch, $\kappa_{o,j}$ is the curvature of the j^{th} notch of the outer tube, and d_j is the distance between the axis offsets of the corresponding j^{th} notches on the inner and outer backbones.

To solve the forward kinematics problem, this equation must be solved numerically to find the array of κ_o values for a given q. In addition to satisfying this kinematic equation, the set of curvatures must also satisfy the requirement that τ is constant throughout the backbones (since friction is assumed to be negligible). This provides us with $n + 1$ variables $(\kappa_{o,1}, \kappa_{o,2}, \ldots, \kappa_{o,n}, \tau)$ and $n+1$ equations (Equation (8) and Equation (7) for $j = 1 \ldots n$). For actuation in the negative direction, which is defined as the inner tube being pushed through the outer tube, this must be modified. Once translation in this direction is large enough, the solid segment of tube below the base of the first notch of the inner tube prevents the first notch of the outer tube from bending. In this case, the number of variables is reduced by one, removing κ_o and τ of the first notch from the set of equations and unknowns. One way to mitigate this effect is to put an additional notch on the base of the inner tube to allow bending below that rigid section.

Once the outer tube curvatures are known, we can rearrange Equation (4) for the j^{th} notch to find the centerline curvature, κ_j:

$$\kappa_j = \frac{\kappa_{o,j}}{1 + \gamma_{o,j} \kappa_{o,j}}. \tag{9}$$

Since the outer tube notch length remains constant as the notch bends, the centerline length l_j over the notch changes with the curvature according to

$$l_j = \frac{h_j}{(1 - \gamma_{o,j} \kappa_j)} \tag{10}$$

for each notch. Because this centerline length is actuation direction dependent, lengthening for positive κ_j and shortening for negative ones, the CPPR will have an asymmetric bending workspace when the inner tube is pushed and pulled with respect to a fixed outer tube.

The transformation from the base of notch j to the base of notch $j + 1$ consists of a constant curvature bending

transformation

$$\boldsymbol{T}_{b,j} = \begin{bmatrix} \cos(\kappa_j l_j) & 0 & \sin(\kappa_j l_j) & (1-\cos(\kappa_j l_j))\,\kappa_j^{-1} \\ 0 & 1 & 0 & 0 \\ -\sin(\kappa_j l_j) & 0 & \cos(\kappa_j l_j) & \sin(\kappa_j l_j)\kappa_j^{-1} \\ 0 & 0 & 0 & 1 \end{bmatrix} \tag{11}$$

followed by a rigid translation

$$\boldsymbol{T}_{r,j} = \begin{bmatrix} 1 & 0 & 0 & 0 \\ 0 & 1 & 0 & 0 \\ 0 & 0 & 1 & c_j \\ 0 & 0 & 0 & 1 \end{bmatrix}. \tag{12}$$

Then, the transformation from the base of the first notch to the tip is

$$\boldsymbol{T} = \prod_{j=1}^{n} \boldsymbol{T}_j = \prod_{j=1}^{n} \boldsymbol{T}_{b,j}\boldsymbol{T}_{r,j}, \tag{13}$$

fully defining the position of the robot in space using the relative tube translation, q.

F. Summary of Model Equations

Once the geometric parameters of the design, namely d_j and l_j, are known, calculating the kinematics can be done one of two ways: with Equation (7) (solved independently for each $\kappa_{o,i}$) if the tension is dictated, or Equation (8) (solved simultaneously for each $\kappa_{o,i}$ and τ) if tube base displacement is dictated. From there, Equations (9) through (13) provide the robot position and orientation along the length.

G. Validation (Verification) of Beam Model Assumptions

The primary assumptions underlying the kinematic model developed in the previous section are (1) that the uncut tube sections behave as rigid bodies, and (2) that the cut sections undergo simple bending as beams. But if the cuts are very close together, or have small width (h) or depth (g), these assumptions may become less valid because the uncut sections may undergo some deformation, and additional deformation modes may occur in the cut sections. To evaluate how these effects may affect model accuracy, we performed a parametric study comparing these geometric assumptions to data from static finite-element analysis (FEA) of a large set of notched tubes under a pure bending load using Autotdesk Inventor Stress Analysis. We calculated the effective neutral axis γ of each tube from the FEA calculated displacements across the tube. We then compared these to the neutral axis that would be predicted by our model assumptions. Since the rigid sections are assumed not to deform, the model-predicted neutral axis is simply the neutral axis of the cut segments (given in [24]) and does not change with notch width (h) or spacing (c), whereas the FEA results account for any rigid segment deformation. Note that the effective neutral axis is the the primary parameter affecting kinematic model accuracy, as it appears in or affects nearly every equation. We simulated five different configurations of width and spacing, and a range of notch depth values for each configuration. The parameters g, h, c, and γ are nondimensionalized by dividing by the outer diameter of the tube, i.e. $g^* = g/OD$, $h^* = h/OD$, $c^* = c/OD$, and $\gamma^* = \gamma/OD$. Simulations were performed on tubes with an outer diameter of 3mm and a wall thickness of 0.1mm. Results are shown in Figure 5. The model γ^* converges to the FEA γ^* as h^* increases and c^* decreases; model agreement also increases as g^* increases for all h^*-c^* configurations. This supports the main kinematic assumption, particularly for designs where $c \leq h$. However, we cannot make c too small or h too large due to issues of mechanical integrity. In Section VI, we discuss practical limits and other design guidance.

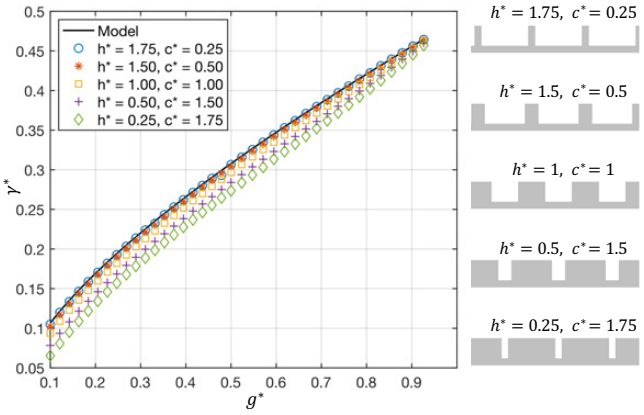

Fig. 5: Model and FEA parametric simulation predictions of γ^* over a range g^* values under different h^*– c^* configurations.

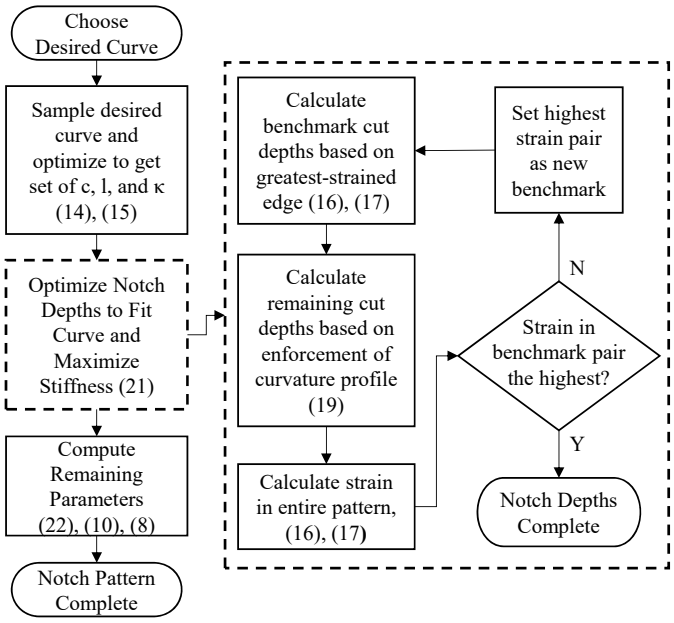

Fig. 6: A flow diagram illustrating the design process for creating an CPPR for a desired actuated shape. Relevant equation numbers are included in parentheses.

III. Notch Design for Variable Curvature Actuated Shapes at Maximal Robot Stiffness

The CPPR can be designed to achieve many actuated shapes by dictating the notch spacing (c), length (h), depths (g_o & g_i), and angle/orientation (ϕ_o & ϕ_i); this actuated shape determines its workspace. Accounting for axial rotation and CPPR actuation, the workspaces in Figure 4 are of designs that only differ by their notch pattern– they have the same material, tube diameters, and number of notches. By changing the actuated shape of the manipulator, the achievable tip angle (shown with arrows) and workspace surface change significantly. All simulations in Figure 4 show results from the workspace of a single-segment, 3-DOF CPPR, which has DOF in (1) bending due to relative tube translation, (2) axial rotation about the base of the tube, and (3) translation of the entire robot. Translation of the entire robot was not simulated, as it simply shifts the entire workspace. Note that using the additional DOF of axial rotation made the workspaces symmetric; this is in contrast to the bidirectional bending range with 1-DOF actuation that is inherently asymmetric, which can be seen in the results in Section IV.In addition to tip position and orientation, the shape of the segment is also important in the context of multi-segment designs, where a second CPPR can be passed through the inner lumen of the first and extended out the tip to create a second, independent bending segment. We demonstrate such a robot in Section V. This section details a single-segment shape design procedure that will be the foundation for future work towards optimal multi-segment CPPR design and control.

The following procedure generates a full CPPR notch pattern from a given desired planar centerline shape by decoupling the problems of (1) fitting the CPPR kinematics to a desired curve and (2) finding the relevant notch parameters to meet those kinematic constraints. Aside from defining the desired curve, the designer needs only to choose the tube geometry, material, number of notches, n, and percentage of the centerline arc length, β, that is composed of the non-notched, non-bending CPPR segments. The design process detailed in this section is summarized in flowchart form in Figure 6, and the steps are as follows:

1) Sample the desired curve to attain a set of desired curvatures, bending section centerline lengths, and rigid section lengths. (Subsection III)
2) Optimize the notch depths for maximum stiffness by using the desired curvatures, section lengths, stock tube geometry, and material strain limit. Iterate on the design based on the strain in all notches until the highest-strained notch experiences the defined strain limit. (Subsection III-B)
3) Compute the remaining notch parameters based on curvatures, depths, and section lengths to complete the design. (Subsection III-C)

The number of notches is left to the designer due to fabrication considerations– a multitude of smaller notches provides better discretization of the curve but takes longer to machine, and may not satisfy some of our modeling assumptions as well. In the case of CNC machining, a designer may be limited by the availability of end mills, and 3D printing must consider the layer discretization and capabilities of the printer. Laser micromachining can easily achieve most designs with high precision. If fabrication limitations are not a significant factor for the designer, they are free to use any optimization technique they wish to sample and fit the curve in place of Step 1, resuming the optimization from that point onward.

The desired actuated shape will generally be defined by some continuous centerline curve $\boldsymbol{p}_d(s)$ in the $x-z$ plane, parameterized by arc length s from 0 to L. The desired curve is sampled at $n+1$ evenly spaced points:

$$s_j = (j-1)\frac{L}{n} \qquad \text{for} \qquad j = 1 \dots n+1.$$

Each discrete segment of length $\frac{L}{n}$ represents a robot segment containing a notched portion followed by a rigid (straight) portion. The lengths of the rigid segments, c, and curved segments, l, are defined by the design input parameter β, which is the proportion of the centerline curve that is considered to be straight:

$$c = \frac{L}{n}\beta, \qquad l_j = \frac{L}{n}\left(1-\beta\right). \tag{14}$$

Starting at the base of the robot, we sequentially find the desired curvature κ_j of each curved segment that minimizes error at each sampled point, which requires that we only solve one nonlinear equation in each step to achieve a set of n κ_j values. Specifically, $\boldsymbol{p}_j$, the position of the end of the j^{th} notched-rigid segment pair, can be calculated as a function of the curvature κ_j using the transformations in Equations (11), (12), and (13). We then select κ_j to minimize e_{j+1}, the component of the error which is normal to the desired curve at s_{j+1}:

$$e_j = N_j^\top \left(\boldsymbol{p}_j - \boldsymbol{p}_d(s_j)\right) \tag{15}$$

where

$$N_j = R_y\left(\frac{\pi}{2}\right)\boldsymbol{p}'(s_j)$$

represents the vector normal to the curve at s_j, $p'(s_j)$ is the arc-length derivative of position at s_j, and $R_y\left(\frac{\pi}{2}\right)$ is the rotation matrix associated with a 90-degree rotation about the y-axis. We use MATLAB's *fsolve* function to accomplish this.

The curve segmentation method described above is only one means of sampling a curve and determining desired curvatures, curve section lengths, and rigid section lengths. This is decoupled from the remainder of the optimization technique such that many other methods could be used to determine those parameters from the curve. Once the set of n κ, l_j, and c_j values are found, the optimization should be used from this point forward.

A. Strain Modeling

The optimization from this point forward is driven by the strain experienced in the notches as they undergo bending, and so we first present modeling for strain that will be used in this optimization. Generally, we want the manipulator to be as stiff as possible while still being able to achieve the desired range of motion within the material strain limits. Thus, we enforce

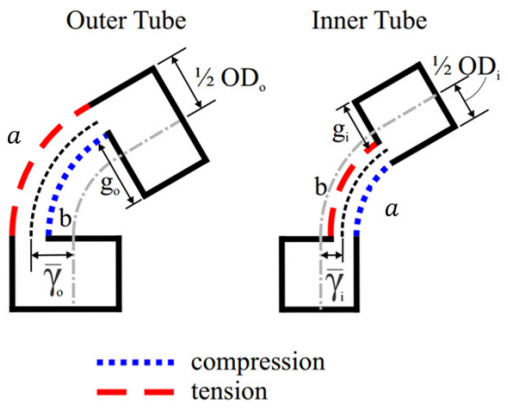

Fig. 7: An illustration of a single notch shows the strain pattern in the inner and outer tubes at the same curvature. The outer tube edge, a, and the inner edge formed by the notch, b, experience strain depending on the direction of actuation. Under positive actuation, the inner tube has tension on b while the outer tube experiences tension in a. The opposite is true for negative actuation.

the maximum tensile strain experienced in any notch is less than the material strain limit ϵ_{max} by a factor of safety FS:

$$\epsilon_{FS} = \epsilon_{max}/FS.$$

This factor of safety can be determined as the designer chooses. A higher factor of safety will lead to a lower strain limit and deeper notches, leaving a thinner remaining backbone section; a lower factor of safety will lead to more shallow notches and a stiffer robot that experiences higher strain. Other factors, such as stress concentrations at the corners, can be used to determine the value of FS.

Per each notch pair, there are four edges experiencing strain, and thus there are four possible magnitudes of maximum strain:

$$\epsilon_j = \left[\left|\epsilon^a_{o,j}\right|, \left|\epsilon^b_{o,j}\right|, \left|\epsilon^a_{i,j}\right|, \left|\epsilon^b_{i,j}\right|\right]$$

The magnitude of the strain experienced under actuation is expressed as

$$\left|\epsilon^a_{x,j}\right| = |\kappa_{x,j}| \left(\frac{OD_x}{2} - \bar{\gamma}_{x,j}\right) \tag{16}$$

and

$$\left|\epsilon^b_{x,j}\right| = |\kappa_{x,j}| \left(\frac{OD_x}{2} + \bar{\gamma}_{x,j} - g_{x,j}\right), \tag{17}$$

where (17) represents the strain in the inner wall formed by the notch, a, (16) represents the strain of the outside edge of the tube, b, and x is a placeholder for either the subscript for the inner tube, i, or for the outer tube, o, and OD_x is the outer diameter of the tube. As illustrated in Figure 7, the outer edge, a of the outer tube is in tension when actuation is positive while the inner edge, b, is in compression. The reverse is true for the inner tube.

B. Notch Depth Optimization

The main driver of the actuated shape is the cut depths, g_o and g_i, and this process must determine these depths based on the desired curvatures. The relationship between the two is defined by Equation (6). To simplify the relationship for this optimization, we assume that $\gamma_o\kappa$ and $\gamma_i\kappa$ are much smaller than unity (i.e. a slender robot or relatively small curvature). In the limit as these values approach zero, $\kappa_o = \kappa_i = \kappa$, (6) becomes linear in κ, and assuming the inner tube tension τ is constant down the length of the manipulator (i.e. assuming no friction), we can write for the j^{th} notch:

$$\kappa_j = \alpha_j \tau \tag{18}$$

where

$$\alpha_j = \frac{d_j}{E_o I_{o,j} + E_i I_{i,j}}.$$

This allows us to linearly relate the geometry of the notch pair to their actuated curvature, and we call α the compliance constant for the notch. From here, we can attain a relationship between all notches in only terms for stiffness, geometry, and curvature:

$$\frac{\kappa_j}{\alpha_j} = \frac{\kappa_k}{\alpha_k} \tag{19}$$

for a given j^{th} notch and $k = 1 \ldots n$.

There is no unique solution for g_o and g_i to achieve a desired κ. To resolve this, we constrain the flexural rigidities of the inner and outer notched segments to be equal to each other:

$$EI_j = E_o I_{o,j} = E_i I_{i,j}. \tag{20}$$

This constraint produced mechanically robust designs in preliminary testing, and it allows the problem to be solved in terms of g_o only.

With these definitions and constraints, our algorithm outlined below effectively solves the following optimization problem:

$$\begin{aligned} &\underset{\{g_{o,1},\ldots,g_{o,n}\}}{\operatorname{argmax}} \left(\min_j EI_j\right) \\ &\text{subject to} \quad \alpha_j = \frac{\alpha_m}{\kappa_m}\kappa_j \quad \forall j \\ &\qquad\qquad \max(\epsilon_j) \le \epsilon_{FS} \quad \forall j \end{aligned} \tag{21}$$

where EI_j is the flexural rigidity of the j^{th} notch, ϵ_{FS} is the material strain limit with a factor of safety, κ_j is the desired centerline curvature from the curve sampling process, and κ_m and α_m are the sampled curvature and compliance constant of the benchmark notch pair, which we define as the pair that experiences the highest-magnitude strain caused by bending. This optimization constrains the maximum strain to be equal to ϵ_{FS} when actuated to the desired curve. The first constraint on α_j in the equation above enforces the desired curvature profile.

There are two variables that must be provided with an initial guess: the characteristics of the benchmark pair and an initial set of g_o values, which must be found numerically because of the high-order relationship between g_o and EI. For the benchmark pair, we assume initially that the outer tube of the notch pair experiencing the highest magnitude curvature, κ_m, will also experience the greatest strain. The initial calculation

assumes the tensile strain will be higher and calculates the notch depth based on (16):

$$\epsilon_{FS} = \left|\epsilon^a_{o,m}\right| = \left|\kappa_{o,m}\right| \left(\frac{OD_o}{2} - \bar{\gamma}_{o,m}\right).$$

Then, we use our relationship in (20) to calculate $g_{i,m}$, use (16) and (17) to evaluate the strain on all edges of the benchmark pair, and iterate the values of $g_{o,m}$ until $\max(\epsilon_m) = \epsilon_{FS}$ for the pair. For the initial guess for the set of g_o values, we use

$$g_{o,j} = g_{o,m} \left|\frac{\kappa_j}{\kappa_m}\right|.$$

In the flowchart in Figure 6, this step is represented in the dashed box. Rather than using a pre-packaged general-purpose nonlinear solver wrapped around our forward kinematics, which was slow to converge and not guaranteed to do so in initial testing, the process in the dashed box accomplishes the optimization for any curve for which the material can handle the strain by finding the required notch depth for the greatest-strained, benchmark pair to exactly meet the strain limit, ϵ_{FS}. This is equivalent to making the notches as stiff as possible while meeting the strain limit constraint. Then, the ratio of curvatures and the compliance constants given as the first constraint in Equation (21) are used to determine all other notch depths. The initial guess we suggest for the benchmark pair assumes the highest-curvature pair of notches experiences the highest strain, but this assumption must be verified; a set of desired κ_j values containing two points with very similar magnitudes of desired curvature (e.g., desired shapes similar to the one used for Design 6 in the experiments) can lead to a lower-curvature notch on the inner tube that is thicker than the strain limit allows, stemming from the EI constraint in Equation (20). One or two iterations of this method typically generates a pattern that remains under the strain limit when actuated to the desired shape.

C. Remaining Parameters

Using the set of desired curvatures, we can define the set of ϕ_o for the notches:

$$\phi_{o,j} = \begin{cases} 0 & \kappa_j < 0 \\ \pi & \kappa_j \geq 0 \end{cases} \tag{22}$$

where ϕ_i is then calculated with Equation (2).

Once the depth pattern is determined, the notch lengths, h, can be found using the relationship between centerline curvature and the outer tube neutral axis offset in Equation (10), resulting in a complete notch profile. From that equation we can see that

$$l_j \leq h_j < 2l_j$$

since $0 \leq \bar{\gamma}_o < \frac{OD_o}{2}$ and $0 \leq \kappa \leq \left(\frac{OD_o}{2}\right)^{-1}$, as self-interference occurs at $\kappa = \left(\frac{OD_o}{2}\right)^{-1}$. The required actuation, q, that attains the desired shape can be calculated with Equation (8), where the set of $\kappa_{o,j}$ values are calculated with Equation (4) and the optimized set of desired κ_j values.

The notch pattern is complete after these final parameters are computed. When using the process as outlined with the suggested initial guesses, this scheme has a convergence time on the order of minutes using non-optimized code in MATLAB and an i7 Intel processor.

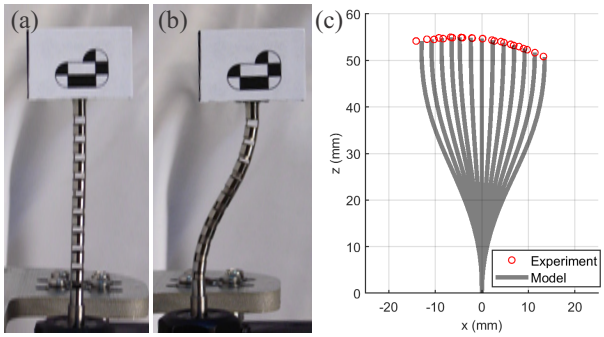

Fig. 8: (a) The unactuated nitinol prototype with position marker at the tip. **(b)** The s-shaped nitinol prototype actuated to its strain limit. **(c)** The experimental results for the tip position of the prototype are shown in the red circles compared to the kinematic model, which shows the manipulator's predicted shape in gray.

IV. Experimental Validation

Seven prototypes of varying cross sections and materials were created to validate the kinematics, and all of them utilized the shape design process to determine the notch pattern. The first experiment tracks the tip position of an endoscopic-scale nitinol prototype to compare to the model prediction; the second set of experiments measure the full shape of six 3D-printed prototypes to compare to both the model prediction of shape and the input desired curve. This section concludes with a discussion of the results and possible sources of error in the shape experiments.

A. Tip Position Experiment in 4mm Nitinol Prototype

An at-scale prototype for endoscopic deployment was built to validate the accuracy of the kinematics model for designs made by laser cutting notches into solid thin-walled tubes. This prototype was 4.02 mm in diameter, small enough to fit in colonoscope tool ports. The shape design algorithm was used to design this robot with a double-bend S-shape to maintain a constant tip angle, and the material strain limit ϵ_{max} for the nitinol prototype was 2% to stay well within the linear range of nitinol's stress-strain behavior. The resulting notch dimensions for the nitinol prototype are tabulated in Table I. The notches were laser cut from superelastic nitinol using a pulsed laser system. Once the notches were laser cut, the exterior of the tubes were sanded with 400 grit sandpaper and their distal ends were adhered using Loctite 430. The tubes are actuated via hollow shaft stepper motors (Nanotec L4118M1804-T5X5) that are attached to a 5mm pitch lead screw. The tubes are attached to the shafts of the stepper motors using ER-16 collets.

To track the tip position of the robot as it actuates across its planar workspace, a marker was attached to the distal end of the robot and was tracked with a MicronTracker H3-60

Nitinol Prototype Notch Parameters					
n	h (mm)	g_o (mm)	g_i (mm)	ϕ_o	ϕ_i
1	2.17	3.63	3.09	π	0
2	2.28	3.70	3.16	π	0
3	2.24	3.68	3.14	π	0
4	2.20	3.65	3.12	π	0
5	2.11	3.55	3.01	π	0
6	2.04	3.32	2.77	0	π
7	2.16	3.62	3.09	0	π
8	2.24	3.68	3.14	0	π
9	2.22	3.66	3.13	0	π
10	2.35	3.72	3.18	0	π

TABLE I: The parameters of the CPPR prototype that vary along the length. For all notches, $c = 3.27$ mm. Tube Geometry : OD_o = 4.02 mm, OD_i = 3.50 mm, $t_o = 0.16$ mm, and $t_i = 0.15$ mm.

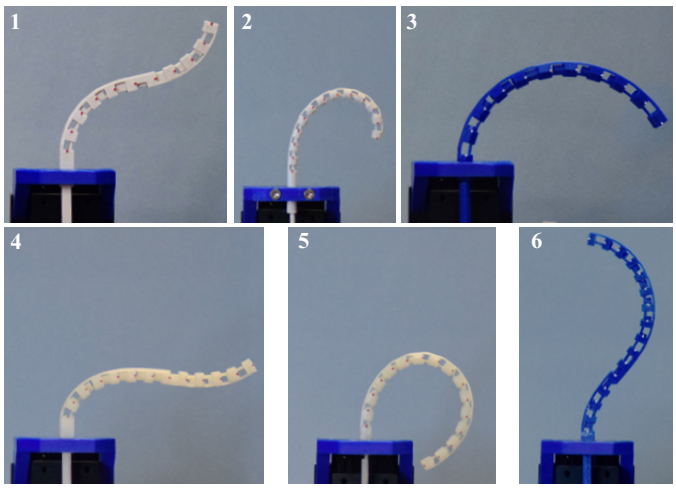

Fig. 9: Designs 1-6, created with the process detailed in Section III, are shown actuated to their desired curve shapes.

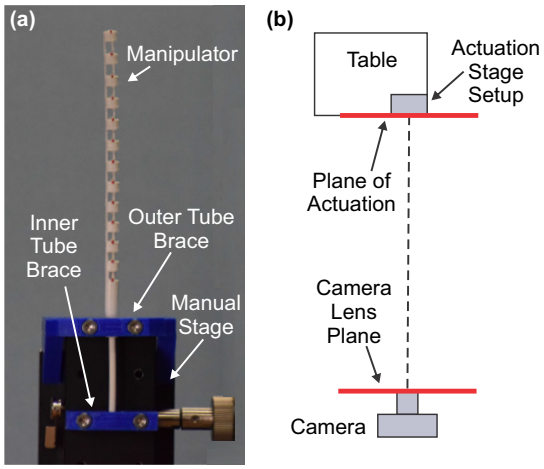

Fig. 10: **(a)** The manipulator was mounted to a linear stage, with the outer tube fixed to the non-moving frame and the inner tube attached to the movable portion of the stage. Small dots were painted on the prototypes to identify the centerline. **(b)** The actuation setup was mounted to an angle brace, clamped to a table, and aligned parallel to a camera approximately 14 ft away to reduce error from perspective.

stereoscopic camera. The outer tube remained fixed while the inner tube was actuated up to 4mm in 0.5mm increments, in both tensile and compressive directions. While actuation force was not measured in this experiment, this prototype could easily be actuated by hand, and the calculated value of the actuation force was 7 N, which is significantly lower than that of traditional concentric tube robots of similar dimensions and range of motion. The maximum position error over the range of actuation was 1.74 mm, and the tip position vs. the model prediction can be seen in Figure 8.

B. Shape Experiments

To further validate the design algorithm rapidly over a wider range of possible shapes and manufacturing methods, six prototypes were designed using the process outlined in Section III and 3D printed on a MAKEiT Pro-M printer using manufacturer-recommended print settings for the given material. The prototypes were 3D printed due to ease of fabrication and availability of low-cost, high-strain materials. We used three materials known to have high strain limits: ColorFabb HT [44], ColorFabb nGen [43], and Nylon Alloy 910 [42]. All six designs pictured in Figure 9 are actuated to their desired shapes. The chosen CPPR parameters used in the optimization are listed in Table II. The tubes were printed horizontally (with layers parallel to the long axis) as opposed to vertically (with layers perpendicular to the long axis of the robot), which tends to fail by layer separation sooner than designs printed horizontally. The pure bending loads experienced during actuation are better supported by horizontal layers running along the tube axis. In addition, vertical printing is more difficult from a process perspective because support material is needed and the tube is less stable when standing vertically.

For all prototypes, the distal notched tube ends were affixed together with cyanoacrylate and the proximal ends were mounted to an MDX-4090-60 linear stage from Optics Focus (0.1 mm resolution, 0.03 mm accuracy) with 3D printed braces, as shown in Figure 10(a). Dots were painted at the base of each notch along the manipulator centerline, which were identified by a small ridge added to the CAD model for the printed designs. A Nikon D3300 DSLR camera was positioned approximately 14 feet from the actuated setup, and a Tamron A17NII lens was used to zoom into the image, reducing image distortion due to perspective to the point at which it was assumed to have negligible effect. Using a remote trigger, a picture was taken at even steps of actuation for each prototype. An image taken in the unactuated state was used to register the base frame of the robot to image space, and measured lengths were used to convert pixel coordinates to millimeters. MATLAB's *ginput* function, which records pixel coordinates from user-input locations, was used to select the painted ridges

Design No.	Cross Section	Material	E (GPa)	ϵ_{max}	ϵ_{FS}	OD_o (mm)	OD_i (mm)	L_{curve} (mm)	β	n	h min-max (mm)	g_o min-max (mm)	q_{max} (mm)
1	Square	ColorFabb HT	1.58	7.00%	5.80%	8.0	5.2	120	0.5	10	6.02-7.44	3.69-7	13.92
2	Circle	ColorFabb HT	1.58	7.00%	6.36%	6.0	2.8	100	0.55	12	3.79-5.33	4.6-5.49	13.44
3	Hexagon	ColorFabb nGen	1.80	4.50%	3.00%	10.0	6.54	150	0.5	10	8.19-8.68	7.26-7.57	16.26
4	Square	Nylon Alloy 910	0.502	18.0%	6.67%	8.0	4.8	120	0.5	12	5.02-6.67	3.98-7.11	13.22
5	Hexagon	Nylon Alloy 910	0.502	18.0%	6.67%	8.0	4.3	150	0.65	15	3.68-4.7	5.4-6.13	17.96
6	Square	ColorFabb nGen	1.80	4.50%	3.91%	8.0	4.8	150	0.45	15	5.55-6.48	5.00-7.04	15.75

TABLE II: Chosen parameters of the CPPR prototypes created using the design process in Section III. All designs had a wall thickness of 1 mm ($t_o = t_i = 1$ mm). The material strain limit is ϵ_{max} per material datasheets [42], [43], [44], and ϵ_{FS} is the strain limit for which the prototypes were designed. The range in h values and g_o values are reported to give an indication of the results of the design procedure.

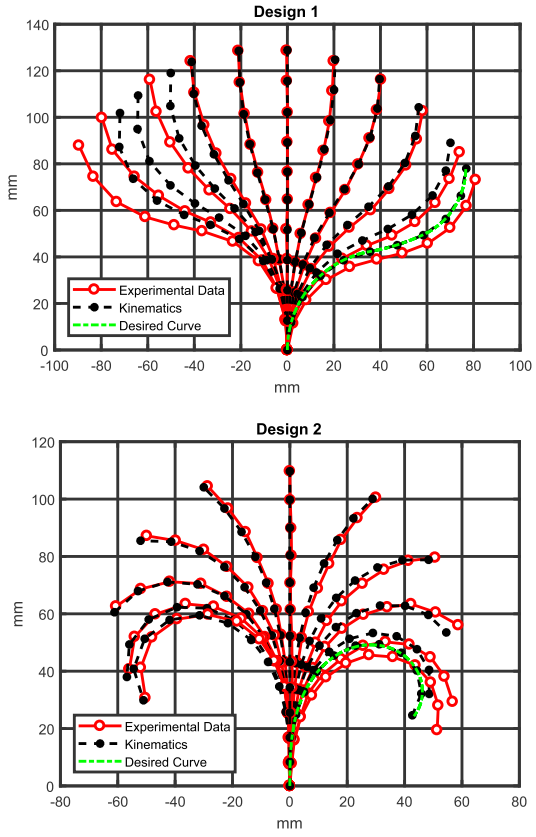

Fig. 11: The experimental results for Designs 1 and 2 for their entire workspace compared to the kinematic model. Interference from a printing artifact caused inaccuracies in both Design 1 (negative half) and 2 (positive half). The desired shape of Design 1 provides near-constant tip orientation. Design 2 exhibits tip-first bending, which is ideal for achieving high angluation in tight spaces.

at the base of each notch, which were typically 2x2 pixels in area on the 1920x1080 pixel monitor. The mm-to-image-pixel scaling for each dataset was calibrated at the start of every experiment. Based on this calibration, the maximum error associated with pixel discretization is calculated as 0.81 mm. This is less than 1% of the robot length for these prototypes.

The plots in Figures 11 through 13 compare the experimental results with the kinematic model prediction for the full robot shape. The experimental results show a single set of measured points for each actuated shape as the robot was incrementally actuated from $q = 0$ to $q = q_{max}$.

C. Results of Shape Experiments

The root-mean-square (RMS) position error of each shape, which used the error of the notch positions compared to the model in each configuration, is provided in Figure 14 as a percentage of robot length. Shape data were recorded at various magnitudes of actuation, $|q|$, as the robot passed from zero to maximum actuation (Pass 1) and from maximum actuation back to zero (Pass 2). The errors provided in Figure 14 were calculated as

$$err = \frac{1}{L}\sqrt{\frac{\sum_{j=1}^{n}\left(\|\mathbf{P}_j - \widehat{\mathbf{P}}_j\|\right)^2}{n}}$$

where L is the length of the robot, n is the total number of notches, $\mathbf{P}_j$ is the recorded position of the j^{th} notch, and $\widehat{\mathbf{P}}_j$ is the position as predicted by the model. In Figure 14, the robot configuration when actuated to its desired curve is marked by the dashed box in the chart for Designs 1-6, which was calculated for each CPPR using Equation (8) and the desired centerline curvatures. Each device was stepped by even increments for the other four configurations. For Designs 1-4 and 6, q was stepped by 3 mm to 12 mm. For Design 5, q was stepped by 4 mm to 16 mm.

The CPPRs overall showed good agreement with the kinematics models, as seen in Figures 11 through 8, which plots the results of Pass 1 as compared to the model prediction. Both the model prediction and experimental data demonstrate the workspace asymmetry, which is dependent on actuation direction as stated in Equation (10) in Section II. These results support the assumption that the printed prototypes behaved as if the material was isotropic, which is what their manufacturers report them to be. As evident in the plots, surface finish artifacts also played a role in error due to frictional effects– in Design 1, the negative half of the workspace is affected by the interaction of surface artifact near the base on the first pass,

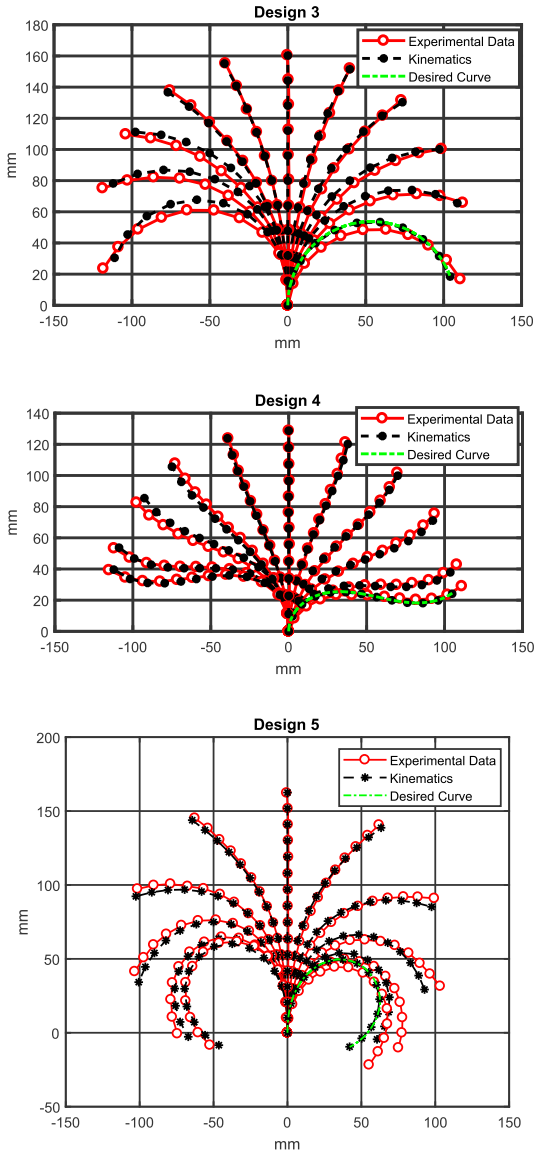

Fig. 12: The experimental results for Designs 3, 4, and 5 for their entire workspace compared to the kinematic model. Design 3 is a constant-curvature arc with a tip angle of 160 degrees. Design 4, with base-first bending, generates a wide-reaching CPPR that has minimal change in tip orientation. Design 5 bends most in the middle, allowing retroflexion.

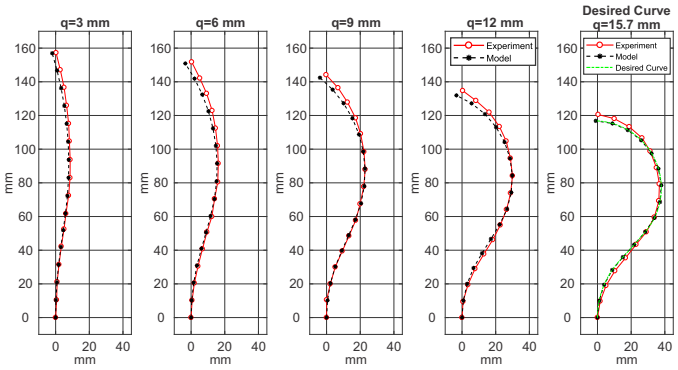

Fig. 13: The experimental results for Design 6 compared to the kinematic model as it steps through actuation. This design changes orientation but has a near-constant position in x.

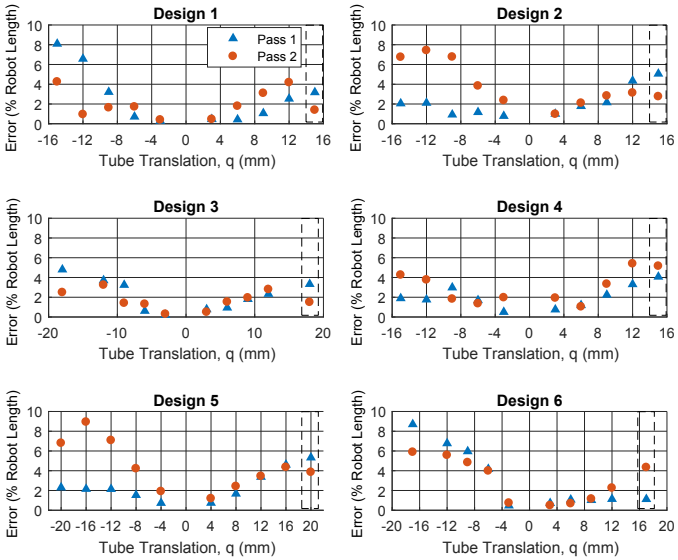

Fig. 14: The RMS error of the shape experiments at multiple configurations. Pass 1 data were recorded as the robot was actuated from zero to its maximum value. Pass 2 data were recorded as the robot returned from its maximum actuation to zero. The error at the desired curve configuration is shown in the dashed box.

which increases friction and causes the robot to bend more at the base and less at the tip.

A small amount of friction was present in all designs, given the variation in position error between Pass 1 and Pass 2, shown in Figure 14. For all prototypes, robots actuated to higher curvatures saw diminishing performance due to friction as compared to lower levels of actuator displacement. As actuation and robot curvature increases, so does the normal force between the inner and outer tubes, causing higher friction forces. This unmodeled effect can become significant at the edges of the manipulator workspace, where effects such as notch misalignment can also begin to effect the results. Most actuated states had similar errors between Pass 1 and Pass 2, though Designs 2 and 5 had clear deviations between the two directions of travel, particularly on the negative half of the workspace. This is likely due to friction causing a hysteresis effect, as rough patches on the tubes pass each other from different directions of travel.

Tube clearances also have some small contribution to the error, as the inner tube will press against the inner wall of the outer tube when actuated, rather than remaining perfectly concentric within it. This increases the distance between the backbones, thus increasing the effective moment arm between the neutral axes of the tubes and leading to smaller angular displacements for the same actuator displacements. This effect causes all notches to bend less than the model predicts for a tube pair with large clearances. Some error can also be attributed to the camera being slightly out of alignment with

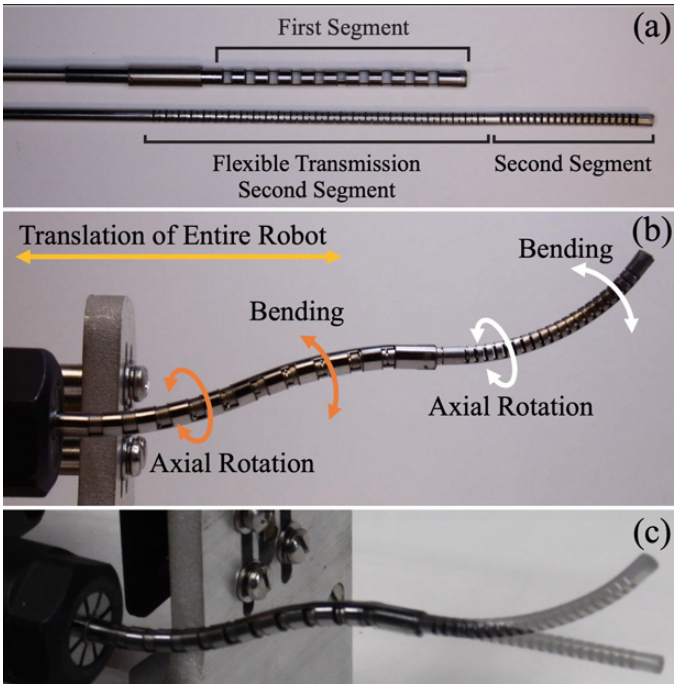

Fig. 15: (a) This nitinol, two-segment robot has an outermost OD of 4.02 mm, and the open inner lumen is 1.844 mm in diameter. The inner tube pair has a flexible transmission segment that exists inside the outer pair and a distal actuating segment. **(b)** The robot has 5 DOF. Both sections rotate and actuate independently, and the entire robot can translate axially **(c)** The first segment actuated independently, showing the second segment in straight and actuated configurations.

the robot bending plane, which means that motion would appear smaller than predicted, as it would be a projection onto the camera plane. Lastly, the discrepancy between the ideal notch parameters used in the model prediction and the as-built parameters of the prototypes, which are affected by the resolution of the 3D printer and settings of the slicer, can contribute to the error seen in the experiments. The model prediction curves consider the machining tolerances, but it does not account for the differences in geometry due to effects of slicing the geometry for printing.

Overall, the 3D-printed, prototype CPPRs that were designed using the process outlined in Section III fit the shape of their desired curves well. RMS shape errors of the robots actuated to the desired shape range from 3.04% (Design 3) to 5.33% (Design 5) when normalized by robot length. While the RMS shape error is a cumulative metric of the error of each measured point along the manipulator per actuated position, the plots in Figures 11 through 13 show a single measurement of each point along the manipulator shape. These results support the assumptions made in our design method, and they show that the process yields designs that attain good shape-fitting results.

V. Multi-Segment Design Demonstration

To demonstrate multi-segment CPPRs, we built a 5-DOF robot out of nitinol, which is shown in the accompanying video and Figure 15. The robot has an outermost diameter of 4.02 mm with a 1.844 mm open lumen diameter. The first segment has tube geometry of $OD_{o,1} = 4.02$ mm, $t_{o,1} = 0.16$ mm, $OD_{i,1} = 3.5$ mm, $t_{i,1} = 0.15$ mm, and the second segment is $OD_{o,2} = 3.0$ mm, $t_{o,2} = 0.1$ mm, $OD_{i,2} = 2.088$ mm, and $t_{i,2} = 0.122$ mm. The entire device can translate, and each segment can independently rotate about its tube axis and bend via push-pull actuation. The inner tube pair contains a segment which is notched symmetrically in order to flex easily as the first (proximal) segment is actuated. The open lumen of the CPPR allows additional nesting for further expansion of DOF if desired, with each segment able to move independently as long as the asymmetrically-notched CPPR segments do not overlap with each other.

The notches of this multi-segment CPPR were cut using a 30W pulsed fiber laser system, where the cut depth, g, was specified by arc length along the tube's outer circumference rather than a depth cut into the tube diameter in the manner defined in Figure 2. As pointed out in [29], laser cutting generates an radially-aligned cut edge that behaves slightly differently than the straight-across cut achieved by milling, and the appropriate equations for I and $\bar{\gamma}$ must be used for the calculations. In the video attachment, we demonstrate each degree of freedom for this multi-segment prototype, illustrating that the bending actuation of each segment does not affect the other. We also demonstrate non-planar motions involving simultaneous rotation of the tube pairs in opposite directions while actuated.

VI. Discussion on Design Considerations

The CPPR is a versatile design concept, and creating a prototype requires careful consideration of many factors. Here, based on our experiments, we offer further guidance to help designers narrow down the unknowns and create a successful CPPR. First, material selection should focus on lubricious materials or those compatible with lubricators to combat friction, which impacts accuracy at the edges of the workspace. Also, material selection must consider the relationship between strain, curvature, and notch depth, as shown in Equations (16) and (17).

A maximum notch depth, which corresponds to a minimum backbone width, can be determined from strength requirements or other design factors, and the neutral axis offset created by this notch drives the relationship between curvature and strain. Using the strain limit of a given material, the maximum curvature of a notch of this depth can be calculated with Equations (16) and (17), allowing designers working with a specific material to select an achievable curve. Conversely, if the desired curve cannot be adjusted or reconfigured, one can select a material based on the strain limit as calculated by the maximum desired curvature and notch depth requirements.

The choice of desired curve can also be used to mitigate the effects of friction and interference between the notches. A designer should avoid large changes in curvature that also coincide with a change in notch direction, as this can cause a point contact between an outer-tube notch edge and the inner-tube backbone and can generate significant friction. A single

notch designed for low curvature either before or after the direction change can mitigate this effect with very little change to the overall curve. The curve itself can be used to define certain characteristics of the whole workspace. For example, choosing a curve that has the same tip angle as the unactuated CPPR will yield a constant-angle manipulator that does not change tip angle anywhere in its actuation range. Similarly, a constant curvature arc for the desired centerline curve will lead to an CPPR that will remain constant curvature at all levels of actuation. More study is needed to determine the best curve selection as related to entire spatial workspace, and future work will focus on this.

A curve discretization parameter was introduced in this paper, β, which influences the notch length and defines the notch spacing. It can be changed to slightly modify the desired notch depths (decreasing β increases the notch length, and a longer notch is less stiff in bending). Generally, this value should be kept near 0.5– the simulation study in Figure 5 shows that model assumptions agree well for values of $c \leq h$ ($\beta \leq 0.5$), and increasing β to above 0.5 means each discrete segment of the CPPR has more of its centerline as straight, rigid section than of a bending, actuated portion. The opposite is true for $\beta < 0.5$, and while this leads to more of the curve being influenced by actuation, having large notch lengths increases the risk of the inner tube buckling, particularly for thin, high-curvature notches. Essentially, a large h is the same as increasing the column length when viewed in light of classic Euler buckling. After a pattern is determined, a designer can verify their design will not buckle using the actuation force and the equation for pinned-pinned column loading:

$$h_{cr,j} = \sqrt{\frac{\pi EI_{i,j}}{\tau_{max}}}$$

where $h_{cr,j}$ is the maximum notch length, τ_{max} is the actuation force at the desired curve as calculated by Equation (7), and $EI_{i,j}$ is the stiffness of the notch. The true end conditions for the notch are more constrained than the pinned-pinned assumption since they can support a moment, so this equation provides a conservative measure since pinned-pinned columns fail at lower loads than other end conditions. Generally, with β near 0.5, the notch lengths produced by the design process are much lower than this critical length. If necessary, increasing the number of notches, n, is a simple and straightforward means of reducing h to meet this criteria.

Selecting proper tube clearances is a balance of material, fabrication method, and friction reduction. For the 3D-printed prototypes, additional clearance helped to mitigate the effects of printing imperfections and snags; however, it also leads to lower-than-expected curvatures when actuated, as seen in the Design 5 results. It can also have a detrimental impact on the negative half of the workspace, where the inner tube is pushed through the outer one, and the model accounts for the absence of bending in the first notch. Large clearances allow this notch to bend, and this additional angular displacement at the base of the robot propagates to larger position errors at the tip. The 3D printed prototypes in this paper had radial clearances ranging from 0.4 to 0.6 mm for the printed prototypes. This large clearance is necessary to accommodate uneven edges and artifacts that can result from the printing process. The metal prototypes, given the difference in their fabrication technique, were able to have much smaller clearances overall, as the nitinol prototype has 0.195 mm radial clearance with good experimental results while the second segment of the multi-segment design in Figure 15 has as little as 0.05 mm of radial clearance between the tubes.

VII. Conclusions

A concentric push-pull tube robot can be designed to achieve general shapes, and we have outlined a process to create designs that achieve desired variable-curvature planar shapes in this paper. We also demonstrated a multi-segment design that can achieve out-of-plane motion with two planar segments. A variable-curvature model was presented and agreed well with the experimental results. Tube clearances and friction can be significant factors affecting model accuracy, and these must be carefully considered in the design stage with the selection of an appropriate material, tube geometry, and fabrication method. Future work will include modeling inverse kinematics, 3D spatial modeling, multi-segment designs, FEA strain modeling, and workspace optimization, particularly as it pertains to robot stiffness under external loads.

References

[1] A. B. Clark and N. Rojas, "Assessing the Performance of Variable Stiffness Continuum Structures of Large Diameter," *IEEE Robotics and Automation Letters*, vol. 4, no. 3, pp. 2455–2462, 2019.

[2] A. Al-Ibadi, S. Nefti-Meziani, and S. Davis, "Cooperative project by self-bending continuum arms," *ICAC 2017 - 2017 23rd IEEE International Conference on Automation and Computing: Addressing Global Challenges through Automation and Computing*, no. September, pp. 7–8, 2017.

[3] K. Xu and H. Liu, "Continuum Differential Mechanisms and Their Applications in Gripper Designs," *IEEE Transactions on Robotics*, vol. 32, no. 3, pp. 754–762, 2016.

[4] L. Li, T. Jin, Y. Tian, F. Yang, and F. Xi, "Design and Analysis of a Square-Shaped Continuum Robot with Better Grasping Ability," *IEEE Access*, vol. 7, pp. 57151–57162, 2019.

[5] H. Zhang, M. Y. Wang, F. Chen, Y. Wang, A. S. Kumar, and J. Y. Fuh, "Design and development of a soft gripper with topology optimization," *IEEE International Conference on Intelligent Robots and Systems*, vol. 2017-Septe, pp. 6239–6244, 2017.

[6] J. Burgner, D. C. Rucker, H. B. Gilbert, P. J. Swaney, K. D. Weaver, and R. J. Webster III, "A Telerobotic System for Transnasal Surgery," *IEEE Transactions on Mechatronics*, 2013.

[7] R. J. Hendrick, S. D. Herrell, and R. J. Webster, "A multi-arm hand-held robotic system for transurethral laser Prostate surgery," in *2014 IEEE International Conference on Robotics and Automation (ICRA)*, pp. 2850–2855, IEEE, may 2014.

[8] M. M. Tonapi, I. S. Godage, and I. D. Walker, "Next generation rope-like robot for in-space inspection," *IEEE Aerospace Conference Proceedings*, 2014.

[9] J. Burgner-Kahrs, D. C. Rucker, and H. Choset, "Continuum Robots for Medical Applications: A Survey, IEEE Transactions on Robotics," *IEEE Transactions on Robotics*, vol. 31(6), no. 6, pp. 31(6):1261–1280, 2015.

[10] K. Oliver-Butler, J. Till, and C. Rucker, "Continuum Robot Stiffness under External Loads and Prescribed Tendon Displacements," *IEEE Transactions on Robotics*, vol. 35, no. 2, pp. 403–419, 2019.

[11] F. Renda, M. Giorelli, M. Calisti, M. Cianchetti, and C. Laschi, "Dynamic model of a multibending soft robot arm driven by cables," *IEEE Transactions on Robotics*, vol. 30, no. 5, pp. 1109–1122, 2014.

[12] M. D. M. Kutzer, S. M. Segreti, C. Y. Brown, R. H. Taylor, S. C. Mears, and M. Armand, "Design of a new cable-driven manipulator with a large open lumen: Preliminary applications in the minimally-invasive removal of osteolysis," in *IEEE International Conference on Robotics and Automation*, no. Dm, pp. 2913–2920, 2011.

[13] Q. Hao, Z. Li, H. Yan, G. Li, and B. Su, "A natural orifice soft robot with novel driven method for minimally invasive surgery (MIS)," *2017 2nd Asia-Pacific Conference on Intelligent Robot Systems, ACIRS 2017*, pp. 289–294, 2017.

[14] R. Xie, M. Su, Y. Zhang, M. Li, H. Zhu, and Y. Guan, "PISRob: A pneumatic soft robot for locomoting like an inchworm," in *IEEE International Conference on Robotics and Automation*, pp. 3448–3453, IEEE, 2018.

[15] A. Shiva, A. Stilli, Y. Noh, A. Faragasso, I. D. Falco, G. Gerboni, M. Cianchetti, A. Menciassi, K. Althoefer, and H. A. Wurdemann, "Tendon-Based Stiffening for a Pneumatically Actuated Soft Manipulator," *IEEE Robotics and Automation Letters*, vol. 1, no. 2, pp. 632–637, 2016.

[16] R. E. Goldman, A. Bajo, and N. Simaan, "Compliant Motion Control for Multisegment Continuum Robots With Actuation Force Sensing," *IEEE Transactions on Robotics*, vol. 30, pp. 1–13, aug 2014.

[17] C. B. Black, J. Till, and D. C. Rucker, "Parallel Continuum Robots: Modeling, Analysis, and Actuation-Based Force Sensing," *IEEE Transactions on Robotics*, vol. 34, no. 1, pp. 29–47, 2018.

[18] F. Dewaele, A. F. Kalmar, F. De Ryck, N. Lumen, L. Williams, E. Baert, H. Vereecke, J. P. Kalala Okito, C. Mabilde, B. Blanckaert, V. Keereman, L. Leybaert, Y. Van Nieuwenhove, J. Caemaert, , and D. Van Roost, "A novel design for steerable instruments based on laser-cut nitinol," *Surgical Innovation*, vol. 21, no. 3, pp. 303–311, 2014.

[19] P. E. Dupont, J. Lock, B. Itkowitz, and E. Butler., "Design and Control of Concentric-Tube Robots," *IEEE Transactions on Robotics*, vol. 26, pp. 209–225, 2010.

[20] D. C. Rucker, B. A. Jones, and R. J. Webster III, "A geometrically exact model for externally loaded concentric-tube continuum robots," *IEEE Transactions on Robotics*, vol. 26, no. 5, pp. 769–780, 2010.

[21] E. C. Burdette, D. C. Rucker, P. Prakash, C. J. Diederich, J. M. Croom, C. Clarke, P. J. Stolka, T. Juang, E. M. Boctor, and R. J. Webster III, "The ACUSITT Ultrasonic Ablator: The First Steerable Needle with an Integrated Interventional Tool," *Proceedings of SPIE Medical Imaging*, 2010.

[22] A. L. Orekhov, V. A. Aloi, and D. C. Rucker, "Modeling parallel continuum robots with general intermediate constraints," *Proceedings - IEEE International Conference on Robotics and Automation*, pp. 6142–6149, 2017.

[23] Y. Bailly, Y. Amirat, and G. Fried, "Modeling and Control of a Continuum Style Microrobot for Endovascular Surgery," *IEEE Transactions on Robotics*, vol. 27, pp. 1024–1030, oct 2011.

[24] K. Oliver-Butler, Z. H. Epps, and D. C. Rucker, "Concentric agonist-antagonist robots for minimally invasive surgeries," in *SPIE Medical Imaging*, p. 1013511, mar 2017.

[25] M. Rox, K. Riojas, M. Emerson, K. Oliver-Butler, D. C. Rucker, and R. J. Webster, "Luminal Robots Small Enough to Fit Through Endoscope Ports: Initial Tumor Resection Experiments in the Airways," in *Hamlyn Symposium on Medical Robotics*, 2018.

[26] P. A. York, P. J. Swaney, H. B. Gilbert, and R. J. Webster, "A wrist for needle-sized surgical robots," in *Robotics and Automation (ICRA), 2015 IEEE International Conference on*, pp. 1776–1781, IEEE, 2015.

[27] P. J. Swaney, P. A. York, H. B. Gilbert, J. Burgner-Kahrs, and R. J. Webster, "Design, fabrication, and testing of a needle-sized wrist for surgical instruments," *Journal of medical devices*, vol. 11, no. 1, p. 014501, 2017.

[28] K. W. Eastwood, S. Member, H. Azimian, B. Carrillo, T. Looi, H. E. Naguib, and J. M. Drake, "Kinetostatic Design of Asymmetric Notch Joints for Surgical Robots," in *IEEE/RSJ International Conference on Intelligent Robots and Systems (IROS)*, pp. 2381–2387, 2016.

[29] K. W. Eastwood, P. Francis, H. Azimian, A. Swarup, T. Looi, J. M. Drake, and H. E. Naguib, "Design of a Contact-Aided Compliant Notched-Tube Joint for Surgical Manipulation in Confined Workspaces," *Journal of Mechanisms and Robotics*, vol. 10, no. 1, p. 015001, 2017.

[30] D. Wei, Y. Wenlong, H. Dawei, and D. Zhijiang, "Modeling of Flexible Arm with Triangular Notches for Applications in Single Port Access Abdominal Surgery," in *IEEE Conference on Robotics and Biomimetics*, pp. 588–593, 2012.

[31] J. Kim, W. Lee, S. Kang, K. Cho, and C. Kim, "A needlescopic wrist mechanism with articulated motion and kinematic tractability for micro laparoscopic surgery," *IEEE/ASME Transactions on Mechatronics*, vol. 25, no. 1, pp. 229–238, 2020.

[32] M. S. Moses, R. J. Murphy, M. D. M. Kutzer, and M. Armand, "Modeling Cable and Guide Channel Interaction in a High-Strength Cable-Driven Continuum Manipulator," *IEEE/ASME Transactions on Mechatronics*, vol. 20, pp. 2876–2889, dec 2015.

[33] H. J. Yu, W. L. Yang, Z. X. Yang, W. Dong, Z. J. Du, and Z. Y. Yan, "Hysteresis analysis of a notched continuum manipulator driven by tendon," *Mechanical Sciences*, vol. 9, no. 1, pp. 211–219, 2018.

[34] A. Gao, R. J. Murphy, H. Liu, I. I. Iordachita, and M. Armand, "Mechanical Model of Dexterous Continuum Manipulators With Compliant Joints and Tendon/External Force Interactions," *IEEE/ASME Transactions on Mechatronics*, vol. 22, no. 1, pp. 465–475, 2016.

[35] J. Kim, W.-Y. Choi, S. Kang, C. Kim, and K.-J. Cho, "Continuously variable stiffness mechanism using nonuniform patterns on coaxial tubes for continuum microsurgical robot," *IEEE Transactions on Robotics*, vol. 35, pp. 1475–1487, Dec 2019.

[36] D.-Y. Lee, J. Kim, J.-S. Kim, C. Baek, G. Noh, D.-N. Kim, K. Kim, S. Kang, and K.-J. Cho, "Anisotropic Patterning to Reduce Instability of Concentric-Tube Robots," *IEEE Transactions on Robotics*, vol. 31, pp. 1311–1323, dec 2015.

[37] H. Azimian, P. Francis, T. Looi, and J. Drake, "Structurally-redesigned concentric-tube manipulators with improved stability," in *2014 IEEE/RSJ International Conference on Intelligent Robots and Systems*, pp. 2030–2035, IEEE, sep 2014.

[38] R. Xu, S. F. Atashzar, and R. V. Patel, "Kinematic Instability in Concentric-tube Robots : Modeling and Analysis," in *IEEE RAS & EMBS International Conference on Biomedical Robotics and Biomechatronics (BioRob)*, no. 1, pp. 163–168, 2014.

[39] T. K. Morimoto and A. M. Okamura, "Design of 3-D Printed Concentric Tube Robots," *IEEE Transactions on Robotics*, vol. 32, pp. 1419–1430, dec 2016.

[40] E. Amanov, T.-D. Nguyen, and J. Burgner-Kahrs, "Additive manufacturing of patient-specific tubular continuum manipulators," in *SPIE Medical Imaging, Vol. 9415* (R. J. Webster and Z. R. Yaniv, eds.), p. 94151P, mar 2015.

[41] P. A. York, S. Member, P. J. Swaney, S. Member, H. B. Gilbert, S. Member, R. J. W. Iii, and S. Member, "A Wrist for Needle-Sized Surgical Robots," in *IEEE International Conference on Robotics and Automation*, pp. 1776–1781, 2015.

[42] SD3D Printing, *Nylon 910 Technical Data Sheet (Alloy 910)*, 2015.

[43] Eastman, *Technical Data Sheet Eastman Amphora 3D Polymer AM*, 2015.

[44] Eastman, *Technical Data Sheet Eastman Amphora 3D Polymer HT*, Nov 2015.

Kaitlin Oliver-Butler (S'15, M'20) received the Ph.D. degree in 2020 and the M.S. degree in 2018, both in mechanical engineering from the University of Tennessee, Knoxville, TN, USA, and the B.S. degree in mechanical engineering from Western Kentucky University, Bowling Green, KY, USA, in 2015. She is currently working as a test engineer in the Environmental Control and Life Support Systems (ECLSS) Test group with NASA as a contractor for Qualis Corporation. Her research and professional interests include life support test systems, oxygen recovery processes, human-robot systems, and robotics in challenging environments.

Jake A. Childs (S'19) received the B.S. and M.S. degrees in mechanical engineering from the University of Tennessee, Knoxville in 2017 and 2020, respectively. He is currently working toward the Ph.D degree in mechanical engineering at the University of Tennessee, Knoxville, TN, as a graduate research assistant in the Robotics, Engineering, and Continuum Mechanics in Healthcare laboratory (REACH Lab). His research interests include modeling and design of soft and continuum robots.

Adam Daniel received the M.S. degree in mechanical engineering from the University of Tennessee, Knoxville, TN, USA, in 2020 and the B.S. degree in mechanical engineering from the University of Tennessee, Knoxville, TN, USA, in 2019. He is currently working as an engineering contractor in the proton therapy industry. His research interests include medical devices and robotic surgical systems.

D. Caleb Rucker (M'13) received the B.S. degree in engineering mechanics and mathematics from Lipscomb University, Nashville, TN, in 2006, and the Ph.D. degree in mechanical engineering from Vanderbilt University in 2010, Nashville TN.

From 2011 to 2013, he was a postdoctoral fellow in Biomedical Engineering at Vanderbilt University. He is now an Associate Professor in mechanical engineering at the University of Tennessee, Knoxville, TN, USA, in 2013 where he directs the Robotics, Engineering, and Continuum Mechanics in Healthcare Laboratory (REACH Lab). He received the NSF CAREER award in 2017. His research interests include mechanical design, modeling, sensing, and control of medical robots and soft/continuum robots.